Journal Pre-proof

Application of a temporal decorrelation model using Sentinel-1 SAR data to Detect volcanic ash deposits related to the 2020 Taal volcano eruption

Camilo Naranjo, Pablo Euillades, Guillermo Toyos, Leonardo Euillades, Gustavo Villarosa

Please cite this article as: Naranjo, C., Euillades, P., Toyos, G., Euillades, L., Villarosa, G., Application of a temporal decorrelation model using Sentinel-1 SAR data to Detect volcanic ash deposits related to the 2020 Taal volcano eruption, *Remote Sensing Applications: Society and Environment* (2023), doi: https://doi.org/10.1016/j.rsase.2023.100991.

This is a PDF file of an article that has undergone enhancements after acceptance, such as the addition of a cover page and metadata, and formatting for readability, but it is not yet the definitive version of record. This version will undergo additional copyediting, typesetting and review before it is published in its final form, but we are providing this version to give early visibility of the article. Please note that, during the production process, errors may be discovered which could affect the content, and all legal disclaimers that apply to the journal pertain.

Application of a Temporal Decorrelation Model Using Sentinel-1 SAR Data to Detect Volcanic Ash Deposits related to the 2020 Taal Volcano Eruption

Camilo Naranjo[1,2], Pablo Euillades[1,3], Guillermo Toyos[1,4], Leonardo Euillades[1,3], Gustavo Villarosa[1,2].

[1]CONICET (National Research and Technical Council), Argentina.
[2]IPATEC (Instituto Andino Patagónico de Tecnologías Biológicas y Geoambientales), UNCo, Bariloche, Argentina
[3]Universidad Nacional de Cuyo, Facultad de Ingeniería, Instituto CEDIAC, Mendoza, Argentina
[4]CONAE (Comisión Nacional de Actividades Espaciales), Buenos Aires, Argentina

Corresponding author: Camilo Naranjo (camilo.naranjo@comahue-conicet.gob.ar), San Carlos de Bariloche, Argentina (CP: 8400)

Abstract

Volcanic ash deposits affect buildings, vegetation, and population. After a volcanic eruption, it is critical to detect the areas affected by ash deposits to achieve an advisable management of the emergency. Optical sensors have been widely used to carry out this task, but they are limited by solar illumination and weather conditions. As an alternative, Synthetic Aperture Radar (SAR) data is not affected by those limitations. Recently, a Temporal Decorrelation Model (TDM) that uses SAR data was proposed for detecting and mapping ash deposits, but it has only been applied to L-band data. Today there is available a huge quantity of C-band data acquired by the Sentinel-1 constellation. In this study we applied the TDM to Sentinel-1 data in order to assess its performance for detecting volcanic ash deposits after an eruption. We selected the eruption of Taal volcano in The Philippines on January 12, 2020, as our case study. We computed more than 4,000 interferometric pairs from a dataset of 93 images acquired before, during, and after the eruption. Our results show that TDM can be applied to C-band data, despite the higher temporal decorrelation suffered by them. Our final probability map is consistent with the field evidence reported by the Philippines Institute of Volcanology and Seismology (PHILVOLCS) and the isopachs map reported in the literature. This new application provides a novel framework for the coherence exploitation of C-Band data. Also, this approach could be applied to detection and monitoring of other natural disasters.

Keywords: Ash deposits; Change Detection; InSAR; Sentinel-1; Temporal Decorrelation Model; Volcanic Ash.

1. Introduction

Detection of ash deposits after a volcanic eruption is important to assist the emergency's management. The ash deposits could lead to indirect hazards, such as secondary lahars or debris flows (Martí and Ernst, 2005). Therefore, spotting affected areas by ash deposits is crucial for generation of hazard maps. A powerful tool to generate hazard maps is satellite images, which can collect data from large areas.

Remote sensing of ash deposits has been traditionally based on optical-infrared data captured by passive sensors using several methods, such as visual interpretation and analysis (Harris et al., 1997; Sato et al., 1997; Tanaka et al., 1981; Tucker and Matson, 1985). Quantitative approaches were based on examination of ash deposits reflectance and albedo changes (Möller et al., 2014; Urai et al., 2001). A more recent strategy has used NDVI (Normalized Difference Vegetation Index) (Easdale and Bruzzone, 2018; Orynbaikyzy et al., 2023). Those methods based on satellite data from passive sensors have provided satisfactory results. However, this kind of sensor is limited by the presence of meteorological clouds and ash plume during a volcanic eruption.

On the other hand, active sensors, such as Synthetic Aperture Radar (SAR) can acquire Earth surface data independently of solar illumination and weather conditions. Therefore, SAR instruments would constitute an interesting alternative for the identification of volcanic ash deposits (Euillades et al., 2021; Massonnet and Feigl, 1998). The detection of ash deposits using SAR images has been addressed in previous works by means of a broad spectrum of data processing and analysis techniques, such as: (a) Visual interpretation of backscatter intensity. The intensity values are strongly modified because of accumulation of ash on the ground (Canisius et al., 2003). And visual interpretation of multi-temporal RGB compositions where the pre-eruption image is assigned to the red channel, whereas the post-eruption image is assigned to green and blue channels (Sasaki et al., 2012). (b) Change detection that uses the image difference of pre- and post-eruption images (Nakano et al., 2010; Terunuma et al., 2005). (c) SAR polarimetry that includes direct- and cross-polarized data analysis and Pauli decomposition (Sasaki et al., 2012; Solikhin et al., 2015). (d) SAR interferometry (InSAR) and change detection combination. This combination is based on the difference between digital elevation models (DEMs) and interferograms. It aims to get information about a ground surface deformation caused by ash deposits (Canisius et al., 2003; Terunuma et al., 2005). (e) Change detection that uses interferometric coherence maps. Coherence maps are a by-product of differential SAR Interferometry (DInSAR) processing (Canisius et al., 2004; Terunuma et al., 2005).

These methods attempt to detect areas affected by ash deposits focusing on identifying changes between satellite data acquired before, during and after an eruption. However, changes could be related not only to volcanic ash deposits but also to natural, random, or seasonal effects. Therefore, these methods' results might be ambiguous.

An alternative methodology has been proposed by Jung et al (2016). They proposed a Temporal Decorrelation Model (TDM), which intends to discriminate changes related to ash deposits from changes due to other phenomena, based on a time series of interferometric coherence maps. A recent assessment has shown that the TDM has better performance than traditional methods, such as change detection using backscatter intensity or coherence difference (Jung and Yun, 2020). However, the first and unique TDM study reported in literature aimed to survey the ash deposits, was applied to the Shinmoedake volcano (Japan) eruption in January 2011 (Jung et al., 2016). This experiment used a series of 22 SAR images acquired by the Phased-Array L-band Synthetic Aperture Radar (PALSAR) aboard the ALOS satellite.

Today there is a huge amount of SAR data available from other sensors like Sentinel-1, among others. Sentinel-1 is a constellation of two polar-orbiting satellites with C-Band SAR instruments on board, that belongs to the Copernicus Programme and European Space Agency (ESA). (https://sentinel.esa.int/web/sentinel/missions/sentinel-1). It is attractive because it provides worldwide open access SAR data with a revisit time of 6-12 days. Furthermore, the Sentinel-1 mission has been active since October 2014; so, it has a steady and long-term data archive. However, C-band data suffer higher temporal decorrelation than L-band data, particularly in areas with vegetation (Hagberg et al., 1995; Orynbaikyzy et al., 2023; Wei and Sandwell, 2010; Zebker and Villasenor, 1992), which could potentially impair the TDM methodology to properly detect and map ash deposits. The purpose of this study is to assess the TDM methodology performance for detecting and mapping ash deposits profiting the Sentinel-1 C-band SAR dataset. This novel application may expand not only the methodology to other datasets but also provides insights of its robustness.

We selected the January 2020 eruption of Taal volcano, located in the Philippines, as our case study. The eruption generated large ash deposits reaching an area of around 8600 km^2 (Balangue-Tarriela et al., 2022). The area surrounding the volcano is interesting for our experiment because they have dense coverage of thick vegetation. Our results were assessed using the official field evidence reported by the Philippines Institute of Volcanology and Seismology (PHILVOLCS) and the isopachs map reported in the literature (Balangue-Tarriela et al., 2022). This paper is organized as follows: Section 2 introduces readers to a review of the decorrelation phenomenon, the concepts of TDM and its model parameters calculation, and the basics of probability calculation. Section 3 describes the study area and the Taal Volcano eruption in 2020; this section also details the dataset and techniques used to compute the interferometric coherence maps. Section 4 shows the results of the implementation of TDM and probability calculation. Finally, sections 5 and 6 report the discussion and conclusions of the study, respectively.

2. Temporal Decorrelation Model
2.1. Interferometric Decorrelation
In a coherent radar system, two signals are correlated when each one results from the same interaction with scatterers located in the area illuminated. If the signal-target interaction is different, they will be uncorrelated, leading to the phenomenon called decorrelation. Decorrelation between Synthetic Aperture Radar (SAR) signals has been extensively studied in the past by Zebker and Villasenor (1992). They demonstrated that decorrelation phenomenon in SAR data can be generated by four factors, such as orbital separation (geometric), thermal noise, illuminated volume, and time.

Geometric decorrelation is related to the distance between the antennas that acquire the image pair known as spatial baseline (Gatelli et al., 1994; Hanssen, 2001). Thermal decorrelation is related to the hardware system noise. It can be considered negligible for the currently operating sensors. Volume decorrelation depends on the penetration of the radar waves, which is related to the wavelengths and the scattering medium (Hanssen, 2001; Weber Hoen and Zebker, 2000). Temporal decorrelation is introduced by changes in the illuminated area between the images acquisition. The signal received by the sensor is a random process, which is determined by the

dielectric and physical structure of the individual scatterers. As the location and physical properties of a scatterer might vary in time, the signal is time-variant too. Hence, the temporal decorrelation is related to the type of land cover present in the scene (Hagberg et al., 1995; Wei and Sandwell, 2010). The temporal decorrelation implies that two images will not be highly correlated if the changes over time between acquisitions are faster than the sensor-data acquisition cycle. Thus, the amount of decorrelation allows us to characterize surface changes that occur at time scales of sensor-data acquisition cycle, such as vegetation growth or disruption, soil moisture-induced effects, ash deposits, snow cover, and so on (Wei and Sandwell, 2010; Zebker and Villasenor, 1992).

The degree of correlation between two SAR images is quantified through a metric known as interferometric coherence. Coherence is defined as the amplitude of the complex cross-correlation coefficient, as expressed by the following equation (1) (Hanssen, 2001):

$$\gamma = \frac{E\{S_1 \cdot S_2^*\}}{\sqrt{E\{|S_1|^2\} \cdot E\{|S_2|^2\}}} , 0 \leq \gamma \leq 1 \qquad (1)$$

where S_1 and S_2 are the images and $E\{\cdot\}$ is the expectation operation. It takes values between 0, meaning no correlation and 1, perfect correlation. Coherence is retrieved from the pair of co-registered images with dimensions $n \; x \; m$ pixels. Therefore, a coherence value is assigned to each pixel generating coherence maps.

2.2. Model rationale

TDM tries to represent the evolution of temporal decorrelation in time. So far, most models developed in literature focus on retrieving information on vegetation structure (Fabio, 2007; Lavalle et al., 2012; Lombardini and Cai, 2014; Zebker and Villasenor, 1992). Those models are based on the hypothesis that temporal decorrelation is due to random motion of the scatterers' elements.

The TDM implemented in this work is represented by equation (2) and considers that the temporal decorrelation is produced by three different processes (Jung et al., 2016): (1) the random motion of the vegetation structure, (2) the temporally correlated dielectric changes like seasonal changes, and normal decrease of the coherence along time, and (3) the temporally uncorrelated dielectric changes (i.e., random).

$$\gamma_t = \frac{1}{1+\mu} \gamma_{d,time}^v \cdot \gamma_{rand}^v + \frac{\mu}{1+\mu} \gamma_{d,time}^g \cdot \gamma_{d,rand}^g \qquad (2)$$

For each pixel within a coherence map computed from scenes S_1 and S_2 , the temporal coherence (γ_t) is modeled as the sum of two terms: one related with the volume interactions (mainly vegetation, v) and the other one related to the ground interactions (g). The sum is normalized by the parameter μ, which represents the ground to volume ratio.

The volumetric and ground random contributions are represented by γ_{rand}^v and $\gamma_{d,rand}^g$, respectively. Note that those variables are pair-variant, meaning that they will take a different value for each interferometric pair, even if they are composed of scenes separated by the same time span.

The non-random decorrelation, again volumetric and ground related ($\gamma_{d,time}^v$ and $\gamma_{d,time}^g$, respectively), are computed from equations (3) and (4), where ΔT is the time span (or temporal baseline) between scenes S_1 and S_2, τ_g is a characteristic time for the ground-signal interactions and τ_v is the corresponding characteristic time for the volume-signal ones. They are modeled as negative exponential functions, i.e., the coherence decreases over time at a rate regulated by the parameters, which is different for ground and volume. Note that the non-random decorrelation is pair-invariant, so it depends only on the temporal baseline between both scenes, meaning that two different pairs spanning the same time will present the same result.

$$\gamma_{d,time}^v = e^{-\left(\frac{\Delta T}{\tau_v}\right)} \qquad (3)$$

$$\gamma_{d,time}^g = e^{-\left(\frac{\Delta T}{\tau_g}\right)} \qquad (4)$$

2.2.1. Model parameters estimation

Model parameters estimation is in order. Let's consider an area of interest where we count on a number N of coherence maps computed from scenes acquired during a given time period. The area was not affected by abnormal events, in terms of interferometric coherence, during the time span. For example, within it there was no volcanic eruption with related ashfall which would have provoked an abnormal coherence decrease. Based on the coherence maps, let's estimate the model parameters relevant for one pixel.

The parameters to be estimated are three pair-invariant ones (μ, τ_g, τ_v) and two pair-variant ones for each map (γ_{rand}^v and $\gamma_{d,rand}^g$).

In order to estimate the invariant parameters, we assume that, for each temporal baseline, there is at least one pair representing the coherence drop due to the temporally correlated changes. In other words, there are pairs where the random components are not present. As those random components impose an additional coherence drop, the maximum coherence for each temporal baseline represented in the dataset, is a good estimate of the uncontaminated natural coherence. Fig. 1.1. displays the coherence vs. temporal baseline (ΔT) at a selected pixel for over 4000 coherence maps covering a given area. For each ΔT, the coherence takes values within a range due to the random components. The maximum coherence is highlighted by blue points. Considering them, we can rewrite the model of equation (2) as:

$$\gamma_t^{high} = \frac{1}{1+\mu} e^{-\left(\frac{\Delta T}{\tau_v}\right)} + \frac{\mu}{1+\mu} e^{-\left(\frac{\Delta T}{\tau_g}\right)} \qquad (5)$$

5

and the parameters μ, τ_v and τ_g can be estimated using curve fitting techniques for non-linear equations, like Newton's, Secant, Levenberg-Marquardt methods, among others (Dennis et al., 1981; Dennis and Schnabel, 1996).

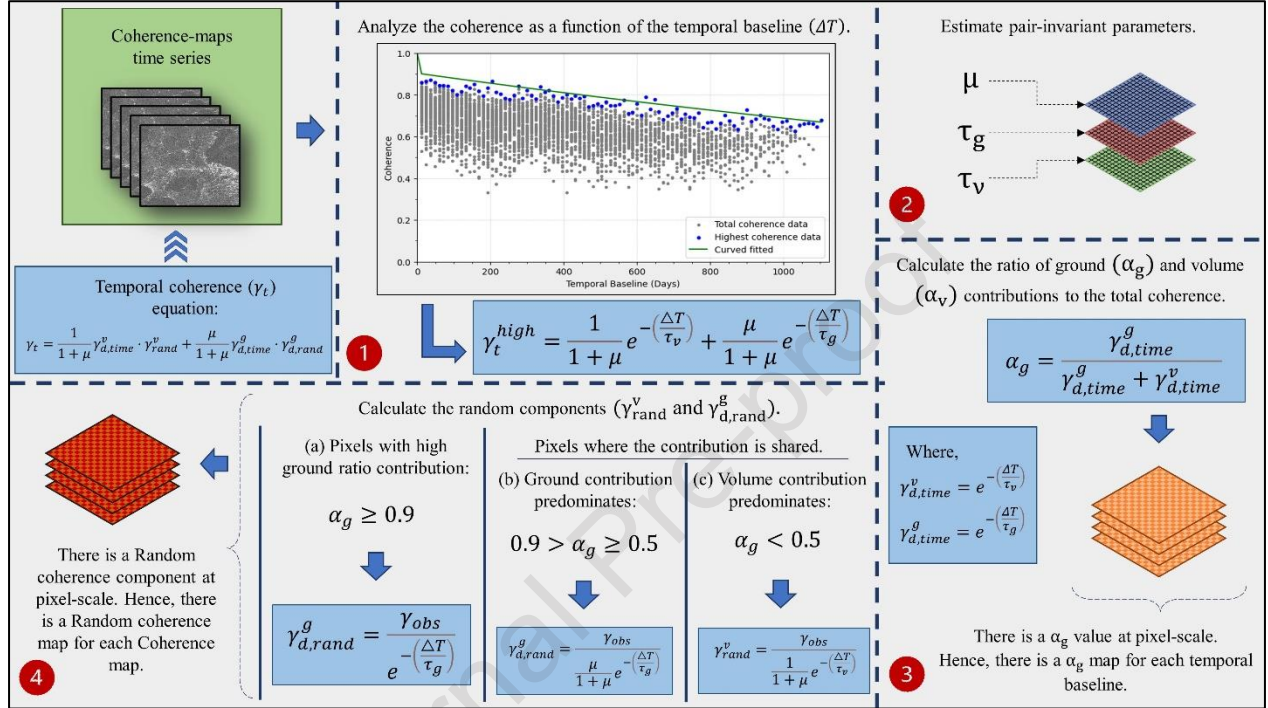To apply the TDM some steps must be followed. These steps are summarized in Fig. 1.

Figure 1. Temporal Decorrelation Model (TDM) workflow. Procedure is applied at pixel-scale within the coherence maps. (1) Analyze the coherence behavior as a function of the ΔT. Then, select the maximum coherence values for each ΔT. (2) Using the maximum values from step 1), estimate pair-invariant parameters (μ, τ_v and τ_g) using non-linear fitting techniques for the highest temporal coherence $\left(\gamma_t^{high}\right)$ equation. (3) Calculate the ratio of ground (α_g) and volume (α_v) contributions to the total coherence with non-random components ($\gamma_{d,time}^v$ and $\gamma_{d,time}^g$) based on pair-invariant parameters estimated in step 2). 4) Calculate the random components (γ_{rand}^v and $\gamma_{d,rand}^g$) according to the three possible value ranges of α_g. For more details see the section 2.2.

The random coherence components (γ_{rand}^v and $\gamma_{d,rand}^g$), as seen in the model equation (Equation 2), represent a unique level of randomness for each pixel, which depends on the nature of the scatterers. As pixels with predominant ground scatterers generate less random outcomes, in terms of coherence, than pixels with vegetation, it is useful to estimate a ratio of ground (α_g) and volume (α_v) contributions to the total coherence. Based on the already estimated pair-invariant parameters, one can compute the non-random decorrelation components using equations (3) and (4). Then, the ratios α_g and α_v are computed as in equations (6) and (7).

$$\alpha_g = \frac{\gamma_{d,time}^g}{\gamma_{d,time}^g + \gamma_{d,time}^v} \qquad (6)$$

$$\alpha_v = \alpha_g - 1 \qquad (7)$$

The random coherence components are computed differently according to the value of α_g. There are three cases: (i) $\alpha_g \geq 0.9$: pixels where the ground contribution is dominant, (ii) $0.9 > \alpha_g \geq 0.5$: pixels where there is some volumetric contribution but the ground one is more important, and (iii) $\alpha_g < 0.5$: pixels where the volumetric contribution is dominant. Using the equation (2), replacing γ_t by the observed coherence for the pair and pixel under investigation and operating, we obtain equations for the random components under the three scenarios (equations 8-10).

$$\forall \, \alpha_g \geq 0.9: \quad \gamma_{d,rand}^g = \frac{\gamma_{obs}}{e^{-\left(\frac{\triangle T}{\tau_g}\right)}} \qquad (8)$$

$$\forall \, 0.9 > \alpha_g \geq 0.5: \quad \gamma_{d,rand}^g = \frac{\gamma_{obs}}{\frac{\mu}{1+\mu} e^{-\left(\frac{\triangle T}{\tau_g}\right)}} \qquad (9)$$

$$\forall \, \alpha_g < 0.5: \quad \gamma_{rand}^v = \frac{\gamma_{obs}}{\frac{1}{1+\mu} e^{-\left(\frac{\triangle T}{\tau_v}\right)}} \qquad (10)$$

Random coherence terms, provide useful information regarding the natural variability of the coherence at a given pixel characterized by its ground coverage. A pixel dominated by ground scattering will present less variability than a pixel with vegetation cover, due to the movement and growing of leaves and small branches. Note that we computed a random coherence value at a pixel for every coherence map, so we can characterize the random behavior of the coherence using those values to compute a probability density function (PDF). Fig. 2 shows the PDF of the random components for a pair of typical pixels during a time period within and without abnormal events, respectively.

2.3. Probability Calculation

Let's call the computed PDF as "reference" one because it characterizes the normal coherence behavior. Next, we must compute another PDF using coherence maps which span an event of interest, for example a volcanic eruption and its associated ashfall covering a region around the volcano. We'll call it as "event" PDF. The coherence behavior in pixels affected by the event will be different than the behavior shall the event did not occur. In order to compute the PDF of the event-affected random coherence, we use maps spanning the event only and employ the already described technique for estimating the model parameters.

The result is another PDF, which can be compared with the reference one. Fig. 2 shows both PDF's for a pair of representative pixels. Note that, in one case (Fig 2a) both PDFs are different,

being the event related one (green bars) notably displaced towards lower values. That pixel is showing that the coherence behavior significantly differs when using maps spanning the event, so we can conclude that it was affected. If the event is an ashfall, the pixels would have been ash covered. Conversely, in the case of the pixel represented in Fig. 2b, both PDFs do not differ, meaning that the pixel was not affected.

One way for quantifying the probability of a pixel being affected by the event is computing the inverse Cumulative Distribution Function (CDF) for the reference (no event) dataset. The CDF represents a proxy of the probability of a pixel with given random coherence to be affected by the event (see red curve in Fig. 2). The mean of the event pairs distribution is projected onto the reference dataset CDF, giving a metric that indicates if both distributions represent the same behavior. This metric is called probability in the original formulation by Jung et al (2016), but note that it should not be interpreted as a classic probability. It is more a relative measure of difference between distributions, where higher value means that random coherence in the event dataset is significantly lower than random coherence in the reference one. The threshold for deciding if a pixel was affected by the event or not is then arbitrary.

In summary, the whole procedure has to be extended to all the imaged pixels, which allows generating a probability map. Pixels with probability greater than an arbitrarily selected threshold are interpreted as being affected, whereas pixels under the threshold were either not affected or the coherence loss in reference conditions is so fast that there is no additional decorrelation detectable.
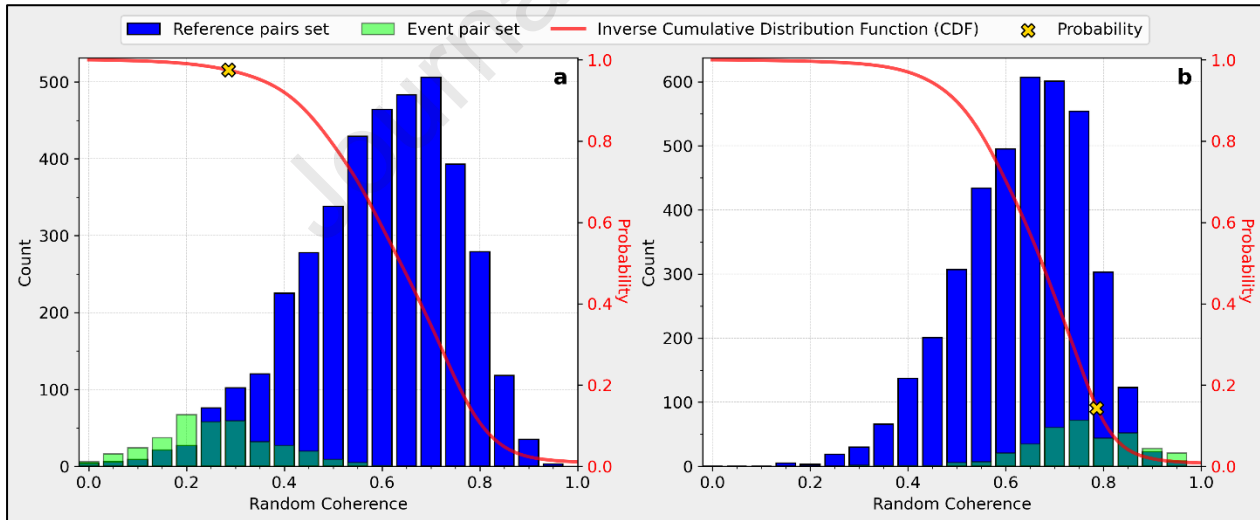

Figure 2. Random coherence distributions of two pixels: (a) high probability (affected by the event) and (b) low probability. The blue and green histograms constitute the distributions of the reference and event pairs datasets, respectively. The red line is the inverse cumulative density function from reference dataset distribution.

3. Study Area and Dataset

3.1. Case Study

We used the January 2020 eruption of Taal volcano, as case study. It was selected due to the diversity of land cover types within the area, magnitude of the eruption, volume and distribution of ash deposits (Balangue-Tarriela et al., 2022), and availability of satellite data.

Taal Volcano is an island in Taal lake within a 25 x 30 km caldera, located South of Manila in The Philippines. This volcano is one of the lowest volcanoes in the world and the country's second one by activity level (Global Volcanism Program, 2020; PHIVOLCS-DOST, 2013). Recent reports of activity include 34 historical phreatic eruptions that occurred between 1572 and 2020, with Volcanic Explosivity Index (VEI) (Newhall and Self, 1982) between 1 and 6, although most of them have been of low explosivity (i.e., VEI = 2) (Delos Reyes et al., 2018; Global Volcanism Program, 2020).

The volcano is composed of more than 40 craters formed during several eruption events that resulted in the accumulation of ashfall and lava flows (Delos Reyes et al., 2018). According to the land cover map shown in Fig. 3 the area is covered by closed forest, cropland, and slightly herbaceous wetlands. Herbaceous wetland corresponds to a lava flow deposit from the eruption that occurred in 1969 (Delos Reyes et al., 2018). Within the processed area (white square shown in Fig. 3) the predominant type of land cover is vegetation: 66.2% of the surface, cropland 19.6%, urban areas 13.4% and others 0.8%. Coverage is relevant because the expected interferometric coherence over vegetation and cropland areas is low.
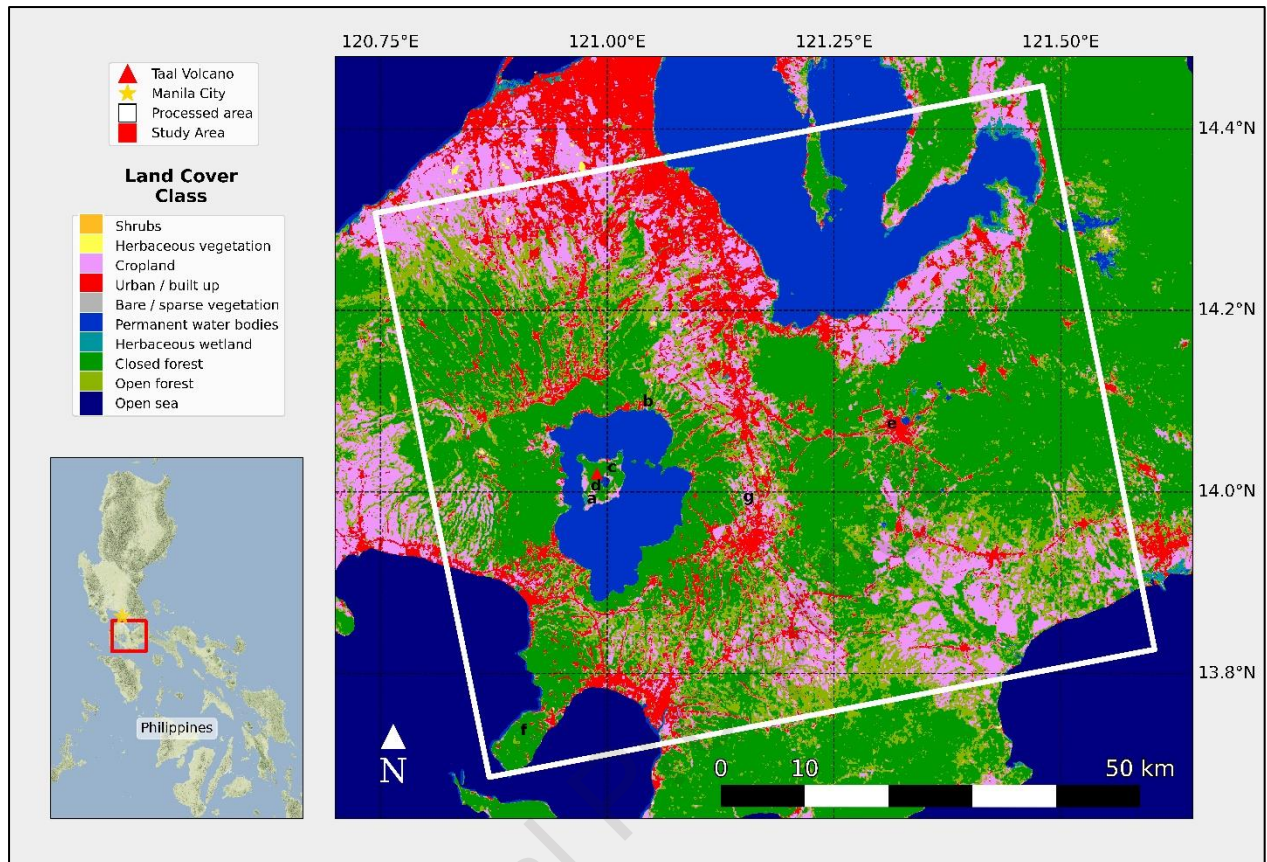
Figure 3. Reference map. This figure is composed by a location map (left bottom), a land cover map of the study area (source: Copernicus Service Information 2019 - https://lcviewer.vito.be/2019) and a footprint of processed SAR images. Also, there are pixels of interest (POIs) labelled with letters as follow: Affected by ash deposits = (a) Lava flow deposits, (b) Urban, (c) Closed vegetation, (d) Open vegetation. Unaffected by ash deposits = (e) Urban, (f) Closed vegetation, (g) Open vegetation.

3.1.1. The January 2020 eruption

On January 12, 2020, at 17:30H (LT) Taal volcano generated a steam-laden tephra column that rose to 15 - 17 km above sea level (PHIVOLCS-DOST, 2020a). The eruption was classified with a VEI 4 and PHIVOLCS reported ashfall at cities located North and Southwest off the main crater (PHIVOLCS-DOST, 2020b, 2020c). The volcano island and areas within a 14 km radius were evacuated and flights suspended at Manila airport (Global Volcanism Program, 2020; PHIVOLCS-DOST, 2020a).

During the first hours, the volcanic ash cloud was dispersed towards the North of the main crater as shown in Fig. 4a. On January 13, the eruption lowered intensity with ash emissions dispersed towards the Southwest of the main crater at around 1 km altitude (PHIVOLCS-DOST, 2020d) (see Fig. 4b.). Emissions continued towards the West and Southwest until January 22, when they ended. On January 22, ash deposits in Taal caldera were remobilized and dispersed towards the Southwest direction by a strong low-level wind (PHIVOLCS-DOST, 2020e). This phenomenon was captured by the astronauts in the International Space Station (ISS) as shown in Fig. 4c.
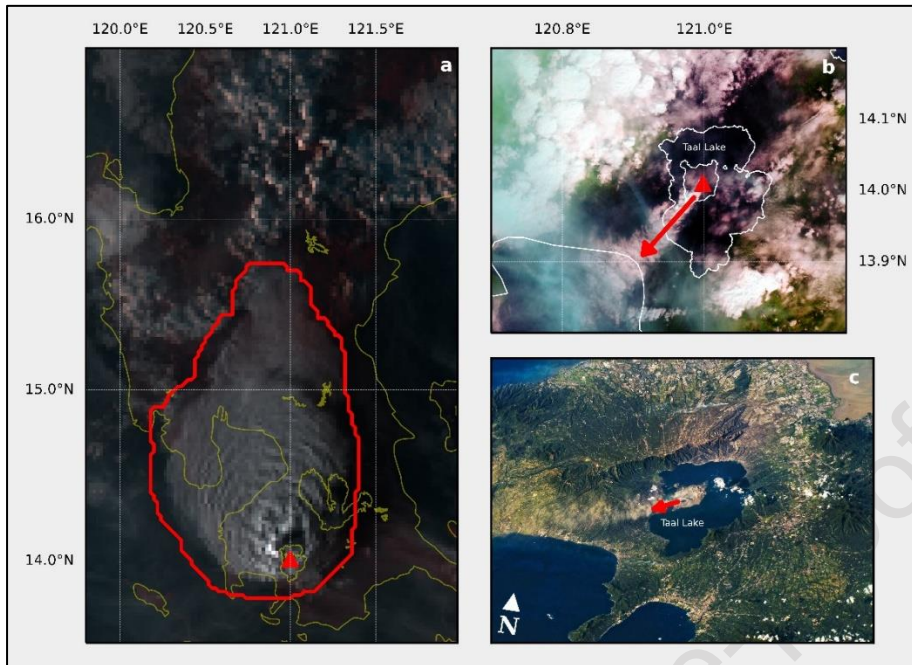
Figure 4. (a) Volcanic ash cloud (red contour) on 12 January at 16:50 (LT). True-color composition, image acquired by the AHI-Himawari-8. (b) Volcanic ash plume from the main crater moving towards the Southwest direction on 13 January at 10:20 (LT). Natural-color composition inspired in a report of Manila Observatory (Flordeliza P. et al., 2020). Image acquired by MSI-Sentinel-2B. (c) Ash remobilization phenomenon taken by the astronauts in the International Space Station (ISS) on 22 January. Image (ISS061-E-138244) courtesy of the Earth Science and Remote Sensing Unit, NASA Johnson Space Center.

3.2. Dataset and processing

The dataset is composed of 93 SAR images acquired in ascending pass (Path 142, Frame 39) by the Sentinel-1 constellation between January 2, 2017, and February 16, 2020. The area of interest is completely within sub-swath 2 and bursts 5-8. The dataset is divided into a subset of 89 images acquired before the eruption and another one composed only of 4 scenes acquired after the eruption. Fig. 5 shows the acquisitions timeline in the context of the eruption. In order to characterize the coherence behavior for a long time period we use all the available scenes. It is possible that similar results could be achieved by using fewer scenes, but we prefer to not unwittingly skew the model by arbitrarily picking some images from the available ones. The pre-eruptive subset was used to compute 3916 interferometric pairs, named reference pairs using all possible combinations. The second subset was used for composing 362 co-eruptive interferometric pairs using all possible combinations of pre-eruptive and post-eruptive images, named event pairs.
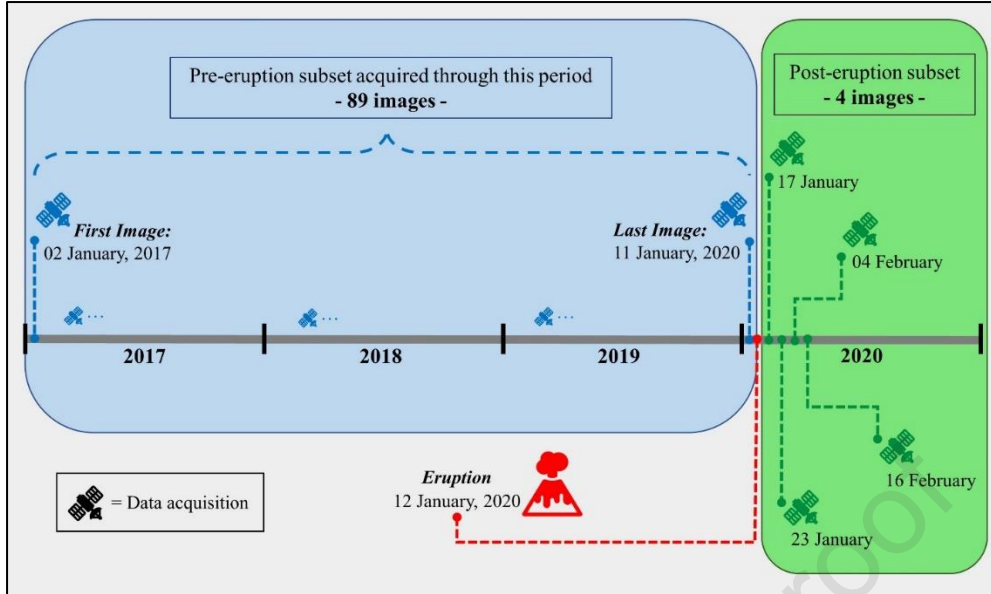
Figure 5.   Data-acquisition timeline of SAR images.

Coherence was computed using a rectangular window of 4 pixels in azimuth by 20 pixels in range, resulting in a ground resolution of ~60 and ~70 m in azimuth and range respectively considering plain terrain. All coherence maps (reference and event pairs) in our study have a dimension of 1250x1100 pixels.

The coherence maps were no compensated for geometric decorrelation because of the orbit of the two satellites from Sentinel-1 constellation are kept within a stringent Earth-fixed orbital tube with a deviation of +/- 100m (European Space Agency (ESA), 2018; Prats-Iraola et al., 2015). The rigorous orbit control is under the care of the Copernicus precise orbit determination (POD) which guarantees the maximum orbit accuracy (Peter et al., 2017), minimizing the geometric decorrelation.

4. Results
4.1. The Implementation of TDM
Let's now estimate the model parameters of the study case relevant for the Taal volcano eruption, following the step-by-step procedure depicted in Fig. 1.

First, let's see the evolution of coherence in time at selected points. Fig. 6 shows the coherence computed from reference pairs as a function of ΔT at four representative points of interest (POIs) characterized with different land cover: 1969 eruption's lava flow (Fig. 6a), urbanized area (Fig. 6b), closed forest (Fig. 6c) and open forest (Fig. 6d). As expected, coherence presents an exponential decrease which is in accordance with temporal coherence equation (2). Note that over former lava flows and urbanized areas the coherence remains high even for time spans longer than 1000 days. Dispersion for pairs with same ΔT is greater in the lava flows than in cities, maybe because the environment in the former areas supports the growing of lower vegetation. In fact, they are classified in Fig. 3 as herbaceous wetlands. By contrast, vegetated areas show low coherence for all temporal baselines. This behavior is in agreement with previous studies

(Hagberg et al., 1995; Orynbaikyzy et al., 2023; Wei and Sandwell, 2010; Zebker and Villasenor, 1992).
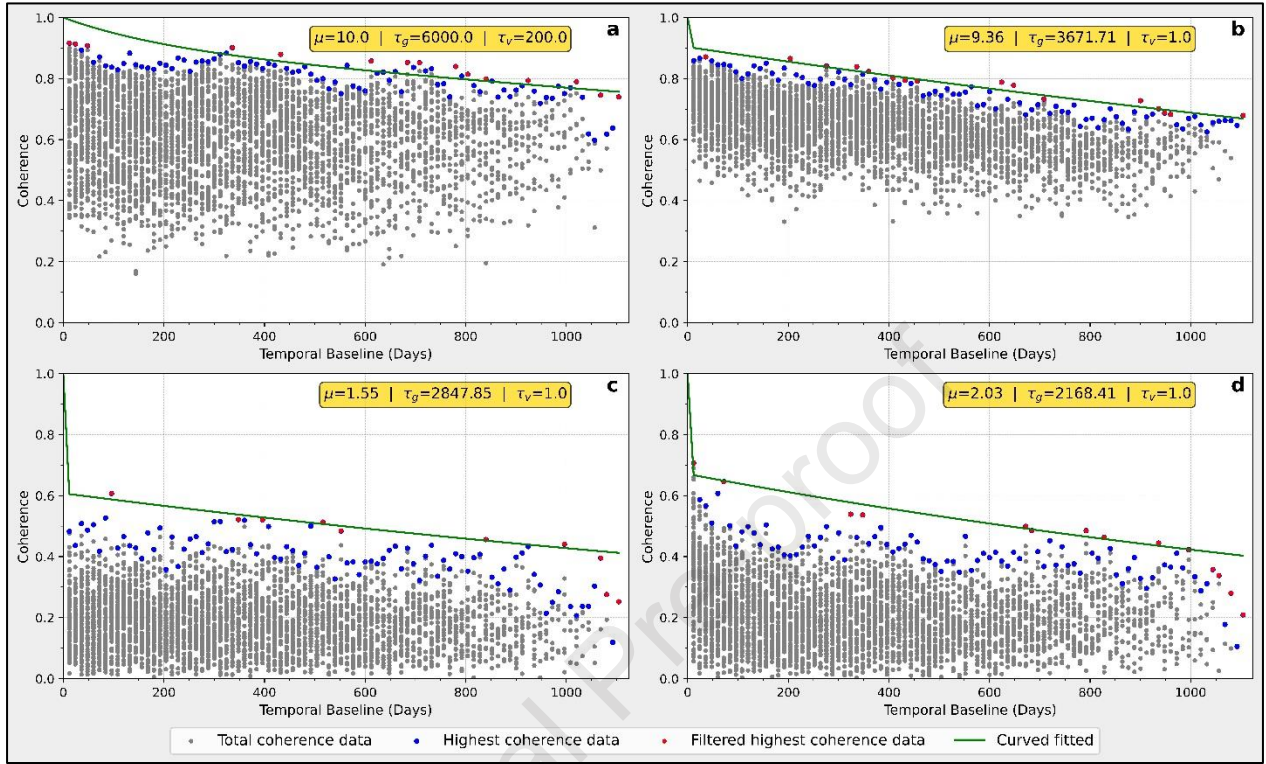

Figure 6. Coherence as a function of temporal baseline for the four representative pixels. (a) Lava. (b) Urban. (c) Closed Forest. (d) Open Forest.

Then, aiming to estimate the pair-invariant parameters (μ, τ_v, τ_g) we must get the values less affected by randomness. The maximum coherence for each ΔT is represented by blue dots in Fig. 6, but they still present some variability which prevents characterizing the long term coherence decline. This is more notorious in the natural environment (lava flows, vegetated areas), when possible seasonal vegetation related effects are present. Subsequently, we filtered that variability by identifying the local maximums (red dots in Fig. 6) and using them for fitting a curve that represents the time evolution of coherence not affected by randomness, i.e., γ_t^{high} of equation (5). We used a robust non-linear least squares curve fitting algorithm which implements the Levenberg-Marquardt method (Dennis et al., 1981; Dennis and Schnabel, 1996). To guarantee the parameters' convergence we established the following empirical constrained bounds: $\{\mu \mid 0.1 \leq \mu \leq 10\}$, $\{\tau_v \mid 1 \leq \tau_v \leq 200\}$ and $\{\tau_g \mid 400 \leq \tau_g \leq 6000\}$.

Figure 7 shows the pair-invariant parameters distribution in the processed area. The ground to volume ratio (μ) can be interpreted as the normalized incidence of ground to volume scattering in the observed coherence. It is expected to be higher in areas where ground scattering mechanisms are dominant over volume scattering ones. In our case, μ takes higher values (>6) in urban areas, intermediate ones (between 4 and 6) over low vegetation areas and old lava flows, and low values (<4) over forested areas, which is consistent with its meaning.
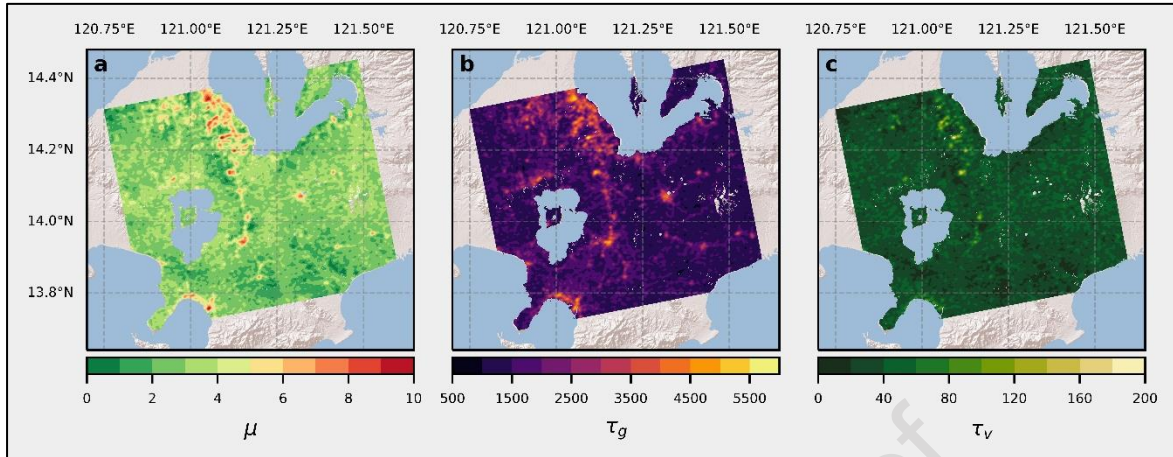
13

Figure 7. Maps of estimated pair-invariant parameters (a) μ map. (b) τ_g map. (c) τ_v map.

Parameters τ_g and τ_v can be interpreted as the characteristic times for the ground and volume scattering mechanisms, respectively. They represent the number of days that produce a temporal coherence decrease of approximately 63%. Ground scattering is characterized by long term coherence (Fig. 7b) whereas volume scattering is responsible for fast coherence drop (Fig. 7c). Note that for a given pixel, the temporal coherence is explained by a combination of both scattering mechanisms, i.e., ground and volume, in a relation governed by the parameter μ (equation 2). So, pixels covered by vegetation are affected by more proportion of volume scattering, causing a coherence loss faster than pixels covered by more stable structures.

Next, we calculated the ratio α_g using equation (6). Note that it is dependent on ΔT, so we computed α_g map for each time span in the reference dataset. In consequence, there are 92 α_g maps for ΔT ranging between 12 and 1104 days. These maps were used for estimating the random coherence components of each reference pair ($\gamma^g_{d,rand}$ and γ^v_{rand}) with equations (8) to (10). Random coherence is the key of TDM to discriminate changes caused naturally from changes caused by the presence of ash deposits. This discrimination is possible because random coherence provides statistical information about how often each pixel is affected by natural or random changes.

Finally, the same procedure, i.e., pair-invariant parameters estimation, α_g calculation and random coherence estimation, was applied to the 362 event pairs. As a result, we have two sets of random coherence components for each pixel, one characterizing the not disturbed coherence evolution, and the other characterizing the coherence affected by eruption related ashfall.

4.2. Random coherence analysis

Now, we use the obtained random coherence distribution for estimating the probability of a given pixel being affected by the "event", which in our case is ashfall. For each pixel, we compute two PDFs using 3916 reference and 362 event random coherence values respectively. Fig. 8 shows them for selected points within the processed area, labeled also in the land cover map of Fig. 3.
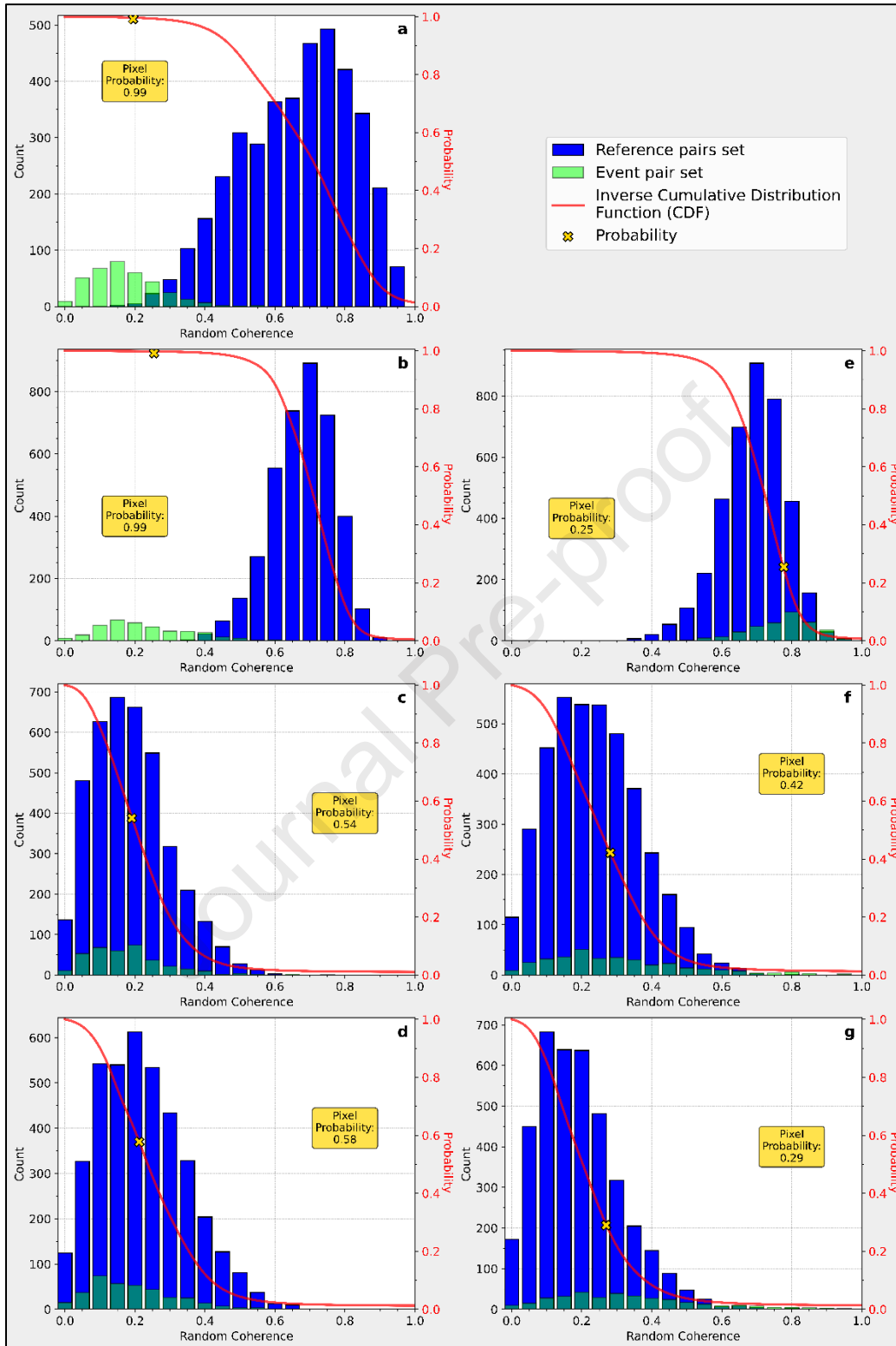
Figure 8.   Probability density functions (PDFs) for pixels with different land cover and contrasting results. Labels correspond to: Pixels affected by ash deposits = (a) Lava flow deposits, (b) Urban, (c) Closed vegetation, (d) Open vegetation. Not affected pixels = (e) Urban, (f) Closed vegetation, (g) Open vegetation.

Pixels affected by ash deposits are presented in Fig. 8(a-b), located at positions with former lava flows and urban coverage respectively. The reference PDFs have means of 0.69 and 0.70, typical of a point where coherence remains high for longer time spans. The event PDFs are clearly shifted towards lower coherence values, indicating a change in coherence behavior that can be interpreted as the result of the studied event. The probability of these pixels being affected by ash deposits, computed as detailed in section 2.3, gives 99%. By contrast, the point represented in Fig. 8e is an urban pixel not affected by ash deposits. Note that both reference and event PDFs have roughly the same mean (0.72 and 0.79, respectively). In consequence, the probability that this pixel is affected by ash deposits is 25%.

Fig. 8c and 8d show pixels covered by vegetation and affected by ash deposits. Both reference and event PDFs are shifted towards low random coherence values and probability at the observed points is slightly higher than 50%. Pixels not affected by ash deposits, shown in Fig. 8f and 8g present similar PDFs, also shifted to low random coherence values. In those cases, the probabilities are 42% and 29%, respectively. In general, at vegetated positions the coherence loss is so fast that for most cases the additional loss due to an event is not detectable.

4.3. Probability map

The probability for every processed pixel is shown in the map of Fig. 9a. There, we superimposed sample points where the Philippine Institute of Volcanology and Seismology (PHIVOLCS) reported ashfall, and isopachs from Balangue-Tarriela et al. (2022). Points in reddish colors are pixels with probability of being affected by ash deposits higher than 60%. Note that they are aligned in Northeast direction, in coincidence with ash deposits revealed by the isopachs and with the plume orientation observed during the eruption from Himawari-8 and Sentinel-2B data (see Fig. 4) (Leung et al., 2020).

Although high probability pixels are oriented in the correct direction, there are also many points of low probability intertwined between them. See, for example, the pattern within the 1.5cm isopach. This result is related to areas with extremely low random coherence where both the reference and event PDFs are shifted to low random coherence values, so no detection is possible. We adopted the following criteria: at pixels where average coherence, computed from the reference pairs, is smaller than 0.2 any additional event-related coherence loss cannot be observed. This is consistent with the observation made by Touzi et al. (1999), where they demonstrate that the coherence estimator is biased towards higher values when coherence is lower than 0.2, a value that slightly changes depending on the number of processing looks. So, we consider that the coherence value obtained at those points is unreliable and mask them out from the probability map.
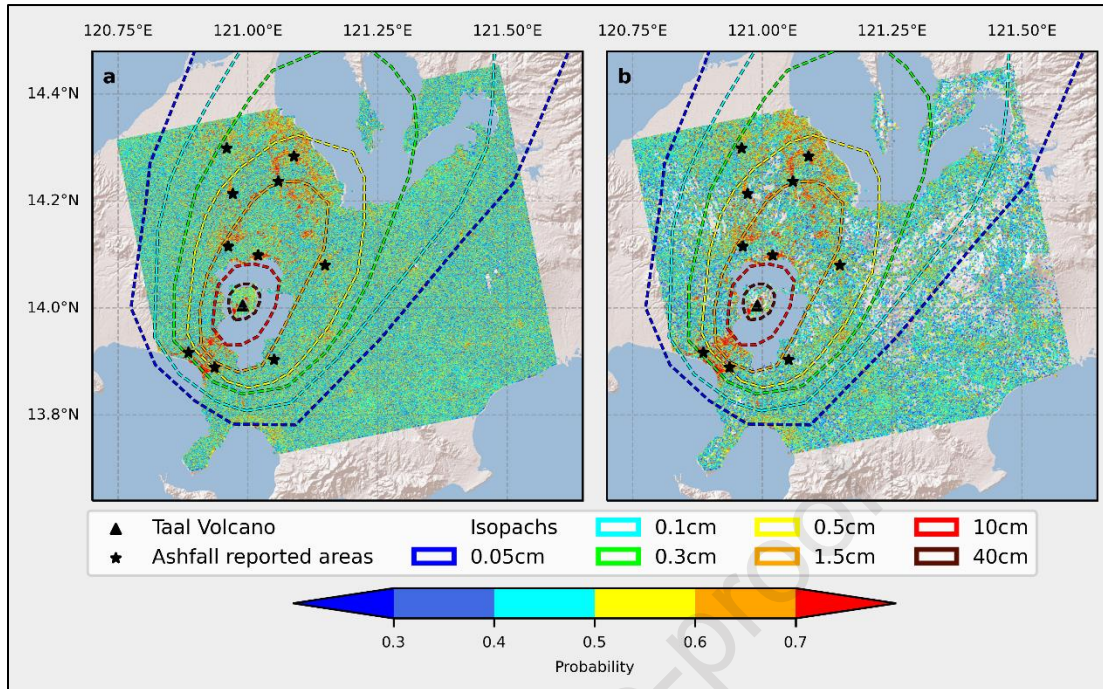
Figure 9. Probability map. a) All pixels (no filter applied). b) Unmasked pixels (pixels with an averaged coherence greater than 0.2). Black stars are the locations where Philippine Institute of Volcanology and Seismology (PHIVOLCS) reported ashfall.

Applying the mask, we obtained the probability map displayed in Fig. 9b. We masked 64% of the total number of processed points. The number of masked points by land cover is shown in Table 1. As expected, the class with more unreliable pixels is the closed forest one (around 73.2%), whereas the urban areas loss only 35.8% of the original points.

Table 1. Comparison between all pixels and unmasked-reliable pixels. Statistical information for each land cover type.

Land cover type[*]	All pixels	Unmasked pixels[**]	Percentage [%] of masked pixels
	Count	Count	
Cropland	213.771	105.249	50.8
Closed Forest	492.725	82.889	83.2
Open Forest	226.782	101.571	55.2
Urban	145.716	93.552	35.8
Others	8.329	3.802	54.4
Total pixels	**1.087.323**	**387.063**	

(*) Land cover types like Permanent water bodies and Open Sea were not included in the analysis.
(**) 700.260 pixels were masked (64.4% of all pixels).

17

5. Discussion

We profit from the availability of the ashfall isopachs to perform the assessment of the accuracy of our results. First, we want to assess if the selected average coherence threshold in the reference dataset is enough to filter out unreliable points. We computed the Receiver Operating Characteristics (ROC) graphs and the Area Under the ROC Curve (AUC) (Fawcett, 2006) to visualize and quantify the model performance for detecting ash within the different isopach levels. The ROC charts display the true positive rate versus the false positive rate, so the detection is better for curves above the diagonal.

Fig. 10 shows the ROC curves for different sets of results, masked using average coherence in the reference dataset of 0.2, 0.5, and 0.75. Different curves within each chart consider only pixels inside the isopachs, for example the red one is representing the performance of the proposed methodology for detecting ash thickness greater than 10cm. Using a coherence of 0.2, our first guess, seems to leave many unreliable points in the dataset, given the curves near the diagonal in Fig. 10a. Instead, a coherence threshold greater than 0.5 enhances only marginally the performance, as can be seen by the AUC metrics (Fig. 10b and 10c). Note that the error in the classification of ash deposits is related to their thickness. This analysis reveals that the methodology performs significantly better for deposits thicker than 1.5cm.
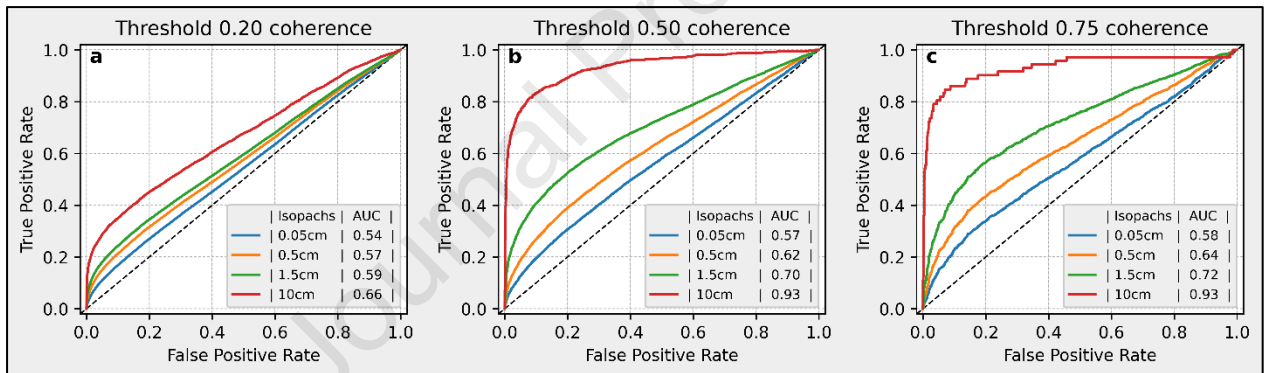

Figure 10. ROC charts for masked points using average coherence in the reference dataset of 0.2, 0.5, and 0.75. Different curves within each chart consider only pixels inside the specific isopach.

Now, we computed the confusion matrix and related metrics. For validation, we consider that all pixels within the 1.5cm isopach are ash covered, and that points outside it are either covered by an ash thickness too thin to be detected or not covered at all. Furthermore, we filtered out all points of average coherence lower than 0.5, according to the analysis of the ROC curves. We performed tests for different probability thresholds, i.e., 0.7, 0.75 and 0.8. See in Fig. 11 the maps of pixels with ash deposits for the different cases.
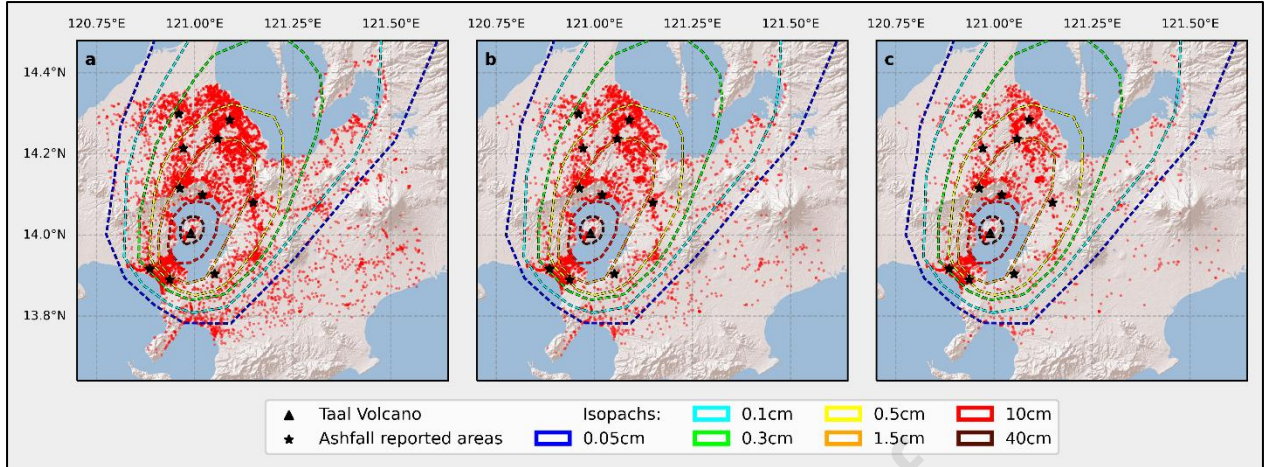
18

Figure 11. Ash deposits map for different probability thresholds (PT). (a) PT = 0.70. (b) PT = 0.75. (c) PT = 0.80.

We focus on the accuracy, that relates the well classified points, positive and negative, to the total number of them in the dataset, and the precision, which computes the percentage of true positives, i.e., pixels classified as ash covered that were really ash covered, to the number of pixels classified as positives by the model. Table 2 shows the computed metrics.

Accuracy is fairly high, higher than 80% for all the analyzed probability thresholds, and increases when more stringent conditions are imposed for considering one of them as affected. Precision also increases for more stringent conditions, but with significantly lower values than accuracy. This metric is particularly affected by the set of positives that are detected outside the area with ashfall, i.e., outside the 1.5cm isopach in our case (see maps in Fig. 11). So, the proposed methodology is detecting many false positives.

Table 2. Accuracy and precision metrics calculated for different probability thresholds*.

Probability Threshold (PT)	Accuracy [%]	Precision [%]	Number pixels classified as positive
0.70	83.79	35.73	8061
0.75	86.06	43.16	5005
0.80	87.2	52.19	2995

*Total number of pixels used in the analysis: 71092

Note that those points are located in high coherence areas, linked to the urban class in Fig. 3. They are points where average coherence in the reference dataset is high, and where a coherence drop is observed in the event dataset. We assume for this study that any coherence drop is related to the studied event, i.e., the volcano eruption. However, given the discussed results, it is probable that other changes which affect the coherence are occurring during the time span of the event dataset. How to minimize the number of no-event-related changes in the event dataset? Note that we formed it by using all available scenes with the sole condition of making co-eruptive coherence maps, which then includes time spans of up to three years. Many changes can occur in such a

19

time period, even in stable areas like cities. So, probably a better strategy is to make a smaller event dataset by restricting the time span between images. However, to make the statistical analysis work, this dataset should have a significant number of samples.

6. Conclusion

We have shown that the TDM can be successfully applied to C-band data, despite the limitations in terms of interferometric coherence when compared with L-band data used to develop the model, i.e., higher temporal decorrelation. Our results were compatible with the expected behavior of temporal coherence in different land covers. We generated a probability map that is consistent with the field evidence, although a deeper study to calibrate some of the model parameters is needed. However, the work demonstrates that C-band data might be useful for mapping ash deposits generated by a volcanic eruption in a very difficult environment in terms of vegetation coverage. This provides a novel framework for the coherence exploitation of C-Band data which takes profit from the huge archive data provided by the Sentinel-1 mission.

Future work should focus on comparing the results using L- and C-band data over the same case study. Some important questions for future studies are to determine the sensitivity of TDM for different SAR data and if it is possible to correlate some parameter to the ash deposits thickness. Another interesting question is about the smallest number of images needed to get high-quality results.

Finally, this methodology could be useful in helping governments and Civil Protection Authorities for the management of emergencies generated by volcanic eruptions. Furthermore, it can be applied to detection and monitoring of other natural disasters, such as wildfires, landslides, and earthquakes.

References

Balangue-Tarriela, M.I.R., Lagmay, A.M.F., Sarmiento, D.M., Vasquez, J., Baldago, M.C., Ybañez, R., Ybañez, A.A., Trinidad, J.R., Thivet, S., Gurioli, L., de Vries, B.V.W., Aurelio, M., Rafael, D.J., Bermas, A., Escudero, J.A., 2022. Analysis of the 2020 Taal Volcano tephra fall deposits from crowdsourced information and field data. Bull Volcanol 84, 1–22.

Canisius, F., Honda, K., Tokunaga, M., Murai, S., Tingsanchali, T., Eiumnoh, A., 2004. Fusion of ascending and descending pass SAR intensity and coherence images for mapping volcanic deposits. Geocarto Int 19, 43–50.

Canisius, J., Honda, K., Tokunaga, M., 2003. Detection of volcanic deposits on mount mayon using SAR interferometry. Geocarto Int 18, 15–19.

Delos Reyes, P.J., Bornas, M.A. V., Dominey-Howes, D., Pidlaoan, A.C., Magill, C.R., Solidum, R.U., 2018. A synthesis and review of historical eruptions at Taal Volcano, Southern Luzon, Philippines. Earth Sci Rev 177, 565–588.

Dennis, J.E., Gay, D.M., Walsh, R.E., 1981. An adaptive nonlinear Least-Squares algorithm. ACM Transactions on Mathematical Software (TOMS) 7, 348–368.

Dennis, J.E., Schnabel, R.B., 1996. Numerical Methods for Unconstrained Optimization and Nonlinear Equations, Numerical Methods for Unconstrained Optimization and Nonlinear Equations. Society for Industrial and Applied Mathematics.

Easdale, M.H., Bruzzone, O., 2018. Spatial distribution of volcanic ash deposits of 2011 Puyehue-Cordón Caulle eruption in Patagonia as measured by a perturbation in NDVI temporal dynamics. Journal of Volcanology and Geothermal Research 353, 11–17.

Euillades, P., Euillades, L., Pepe, A., Mastro, P., Falabella, F., Imperatore, P., Tang, Y., Rosell, P., 2021. Recent advancements in multi-temporal methods applied to new generation SAR systems and applications in South America. J South Am Earth Sci 111, 103410.

European Space Agency (ESA), 2018. Orbit - Sentinel-1 - Sentinel Handbook - Sentinel Online [WWW Document]. URL https://sentinels.copernicus.eu/web/sentinel/missions/sentinel-1/satellite-description/orbit (accessed 7.4.22).

Fabio, R., 2007. Modeling interferogram stacks. IEEE Transactions on Geoscience and Remote Sensing 45, 3289–3299.

Fawcett, T., 2006. An introduction to ROC analysis. Pattern Recognit Lett 27, 861–874.

Flordeliza P., D.C., Patricia Mae J., P., May Celine T.M., V., Laurice P., J., Gemma T., N., 2020. Impacts of Taal Volcano phreatic eruption (12 January 2020) on the environment and population: Satellite-based observations compared with historical records [WWW Document]. Manila Observatory . URL https://www.observatory.ph/2020/04/20/impacts-of-taal-volcano-phreatic-eruption-12-january-2020-on-the-environment-and-population-satellite-based-observations-compared-with-historical-records/ (accessed 12.22.22).

Gatelli, F., Guarnieri, A.M., Parizzi, F., Pasquali, P., Prati, C., Rocca, F., 1994. The wavenumber shift in SAR interferometry. IEEE Transactions on Geoscience and Remote Sensing 32, 855–865.

Global Volcanism Program, 2020. Report on Taal (Philippines) [WWW Document]. Bulletin of the Global Volcanism Network. URL https://volcano.si.edu/showreport.cfm?doi=10.5479/si.GVP.BGVN202006-273070 (accessed 6.27.22).

Hagberg, J.O., Ulander, L.M.H., Askne, J., 1995. Repeat-pass SAR interferometry over forested terrain. IEEE Transactions on Geoscience and Remote Sensing 33, 331–340.

Hanssen, R.F., 2001. Radar Interferometry, Remote Sensing and Digital Image Processing. Springer Netherlands, Dordrecht.

Harris, A.J.L., Butterworth, A.L., Carlton, R.W., Downey, I., Miller, P., Navarro, P., Rothery, D.A., 1997. Low-cost volcano surveillance from space: Case studies from Etna, Krafla, Cerro Negro, Fogo, Lascar and Erebus. Bull Volcanol 59, 49–64.

Jung, J., Kim, D.J., Lavalle, M., Yun, S.H., 2016. Coherent change detection using InSAR temporal decorrelation model: A case study for volcanic ash detection. IEEE Transactions on Geoscience and Remote Sensing 54, 5765–5775.

Jung, J., Yun, S.H., 2020. Evaluation of coherent and incoherent landslide detection methods based on synthetic aperture radar for rapid response: A case study for the 2018 Hokkaido landslides. Remote Sensing 2020, Vol. 12, Page 265 12, 265.

Lavalle, M., Simard, M., Hensley, S., 2012. A temporal decorrelation model for polarimetric radar interferometers. IEEE Transactions on Geoscience and Remote Sensing 50, 2880–2888.

Leung, G.F., Hilario, M.R., Betito, G., Bañaga, P.A., Vincent Topacio, X.G., Cainglet, Z.M., Visaga, S.M., Delos Reyes, I., Olaguera, L.M., Dado, J.M., Cruz, F., Maquiling, J., Obiminda Cambaliza, M., Bernard Simpas, J., Narisma, G.T., Holz, R., Kuehn, R., Eloranta, E., 2020. Taal Volcano 2020 eruption impact on air quality (Part I) | Manila Observatory [WWW Document]. Manila Observatory. URL https://www.observatory.ph/2020/01/17/taal-volcano-2020-eruption-impact-on-air-quality-part-i/ (accessed 5.3.23).

Lombardini, F., Cai, F., 2014. Temporal decorrelation-robust SAR tomography. IEEE Transactions on Geoscience and Remote Sensing 52, 5412–5421.

Martí, J., Ernst, G., 2005. Volcanoes and the Environment, Cambridge University Press. Cambridge University Press.

Massonnet, D., Feigl, K.L., 1998. Radar interferometry and its application to changes in the Earth's surface. Reviews of Geophysics 36, 441–500.

Möller, R., Möller, M., Björnsson, H., Gudmundsson, S., Pálsson, F., Oddsson, B., Kukla, P.A., Schneider, C., 2014. MODIS-derived albedo changes of Vatnajökull (Iceland) due to tephra deposition from the 2004 Grímsvötn eruption. International Journal of Applied Earth Observation and Geoinformation 26, 256–269.

Nakano, Y., Yamakoshi, T., Shimizu, T., Tamura, K., Doshida, S., 2010. The evaluation of eruption induced sediment related disasters using satellite remote sensing-Applications for emergency response, International Journal of Erosion Control Engineering.

Newhall, C.G., Self, S., 1982. The volcanic explosivity index (VEI): an estimate of explosive magnitude for historical volcanism. J Geophys Res 87.

Orynbaikyzy, A., Plank, S., Vetrita, Y., Martinis, S., Santoso, I., Dwi Ismanto, R., Chusnayah, F., Tjahjaningsih, A., Suwarsono, Genzano, N., Marchese, F., Rokhis Khomarudin, M., Strunz, G., 2023. Joint use of Sentinel-2 and Sentinel-1 data for rapid mapping of volcanic eruption deposits in Southeast Asia. International Journal of Applied Earth Observation and Geoinformation 116, 103166.

Peter, H., Jäggi, A., Fernández, J., Escobar, D., Ayuga, F., Arnold, D., Wermuth, M., Hackel, S., Otten, M., Simons, W., Visser, P., Hugentobler, U., Féménias, P., 2017. Sentinel-1A – First precise orbit determination results. Advances in Space Research 60, 879–892.

PHIVOLCS-DOST, 2013. General Information Products, Flyer - Taal Volcano Profile [WWW Document]. URL https://www.phivolcs.dost.gov.ph/index.php/publications/general-information-products (accessed 6.27.22).

PHIVOLCS-DOST, 2020a. TAAL VOLCANO BULLETIN 12 January 2020 07:30 PM [WWW Document]. URL https://www.phivolcs.dost.gov.ph/index.php/volcano-hazard/volcano-bulletin2/taal-volcano/9620-taal-volcano-bulletin-12-january-2020-07-30-pm (accessed 6.27.22).

PHIVOLCS-DOST, 2020b. ERUPTION UPDATE FOR TAAL VOLCANO 13 JANUARY 2020 03:20 AM [WWW Document]. URL https://www.phivolcs.dost.gov.ph/index.php/volcano-hazard/volcano-bulletin2/taal-volcano/9622-eruption-update-for-taal-volcano-13-january-2020-03-20-am (accessed 6.27.22).

PHIVOLCS-DOST, 2020c. ERUPTION UPDATE FOR TAAL VOLCANO 13 JANUARY 2020 04:00 PM [WWW Document]. URL https://www.phivolcs.dost.gov.ph/index.php/volcano-hazard/volcano-bulletin2/taal-volcano/9633-eruption-update-for-taal-volcano-13-january-2020-04-00-pm (accessed 6.27.22).

PHIVOLCS-DOST, 2020d. TAAL VOLCANO BULLETIN 14 January 2020 8:00 A.M. [WWW Document]. URL https://www.phivolcs.dost.gov.ph/index.php/volcano-hazard/volcano-bulletin2/taal-volcano/9636-taal-volcano-bulletin-14-january-2020-8-00-a-m (accessed 6.27.22).

PHIVOLCS-DOST, 2020e. TAAL VOLCANO ADVISORY: 22 JANUARY 2020 04:00 PM [WWW Document]. URL https://www.phivolcs.dost.gov.ph/index.php/volcano-hazard/volcano-bulletin2/taal-volcano/9679-taal-volcano-advisory-22-january-2020-04-00-pm (accessed 6.27.22).

Prats-Iraola, P., Rodriguez-Cassola, M., De Zan, F., Scheiber, R., López-Dekker, P., Barat, I., Geudtner, D., 2015. Role of the orbital tube in interferometric spaceborne SAR missions. IEEE Geoscience and Remote Sensing Letters 12, 1486–1490.

Sasaki, H., Sakagami, M., Fujiwara, S., Sato, T., Honda, K., Haraguchi, M., Kasuga, A., Muraki, H., Iribe, K., Kobayashi, T., 2012. Investigation of the 2011 eruption of Shinmoedake volcano, Kirishima volcanic group, Japan, using RADARSAT-2 SAR data. International Journal of Erosion Control Engineering 5, 80–85.

Sato, M., Ishiguro, E., Fujita, S., Hirata, K., Miyahara, T., 1997. Estimation of aboveground biomass using landsat-5/tm and noaa/avhrr. Journal of Agricultural Meteorology 52, 579–582.

Solikhin, A., Pinel, V., Vandemeulebrouck, J., Thouret, J.C., Hendrasto, M., 2015. Mapping the 2010 Merapi pyroclastic deposits using dual-polarization Synthetic Aperture Radar (SAR) data. Remote Sens Environ 158, 180–192.

Tanaka, Y., Tsuchiya, K., Yamaura, Y., 1981. Detection of volcanic smoke and ash-fall area at Volcano Aso, from Landsat MSS data. Papers in Meteorology and Geophysics 32, 275–290.

Terunuma, T., Nishida, K., Amada, T., Mizuyama, T., Sato, I., Urai, M., 2005. Detection of traces of pyroclastic flows and lahars with satellite synthetic aperture radars. Int J Remote Sens 26, 1927–1942.

Touzi, R., Lopes, A., Bruniquel, J., Vachon, P.W., 1999. Coherence estimation for SAR imagery. IEEE Transactions on Geoscience and Remote Sensing 37, 135–149.

Tucker, C.J., Matson, M., 1985. Determination of volcanic dust deposition from el chichon using ground and satellite data. Int J Remote Sens 6, 619–627.

Urai, M., Kawanabe, Y., Itoh, J., Takada, A., Kato, M., 2001. Ash fall areas associated with the Usu 2000 eruption observed by ASTER. Bulletin of the Geological Survey of Japan 52, 189–197.

Weber Hoen, E., Zebker, H.A., 2000. Penetration depths inferred from interferometric volume decorrelation observed over the Greenland ice sheet. IEEE Transactions on Geoscience and Remote Sensing 38, 2571–2583.

Wei, M., Sandwell, D.T., 2010. Decorrelation of L-band and C-band interferometry over vegetated areas in California. IEEE Transactions on Geoscience and Remote Sensing 48, 2942–2952.

Zebker, H.A., Villasenor, J., 1992. Decorrelation in interferometric radar echoes. IEEE Transactions on Geoscience and Remote Sensing 30, 950–959.

Highlights

- Temporal Decorrelation Model improves the change detection with SAR data.

- Adaptation of a Temporal Decorrelation Model to C-band data.

- C-band data is useful to detect ash deposits generated by a volcanic eruption.

- Novel framework for the coherence exploitation of C-Band data.

Ethical Statement

The authors declare that all ethical practices have been followed in relation to the development, writing, and publication of the article.

Author contributions

CN: Software, Investigation, Data Curation, Writing - Original Draft, Visualization, Validation, Formal analysis.

PE: Conceptualization, Supervision, Validation, Writing - Review & Editing, Formal analysis.

GT: Supervision, Writing - Review & Editing.

LE: Conceptualization, Software, Resources.

GV: Validation.

Declaration of interests

☒ The authors declare that they have no known competing financial interests or personal relationships that could have appeared to influence the work reported in this paper.

☐ The authors declare the following financial interests/personal relationships which may be considered as potential competing interests: